Taylor & Francis
Taylor & Francis Group

LAMINAR CONFINED IMPINGING JET INTO A POROUS LAYER

Daniel R. Graminho and Marcelo J. S. de Lemos

Departamento de Energia—IEME, Instituto Tecnológico de Aeronáutica—ITA, São José dos Campos, Brazil

This work aims at studying laminar impinging jets on surfaces covered with a layer of a porous material. This contribution may provide insight into the design and optimization of heat and mass transfer processes over surfaces. Numerical simulations are presented and the porous substrate is treated as a rigid, homogeneous, and isotropic medium. Macroscopic transport equations are written for a representative elementary volume (REV), yielding a set of equations that is valid for the entire computational domain, including both the porous layer attached to the surface and the fluid layer over the porous substrate. These equations are discretized using the control-volume method and the resulting system of algebraic equations is relaxed using the Strongly Implicit Procedure (SIP) methods. The SIMPLE algorithm is used to handle the pressure–velocity coupling. Results for flow, in both clear and porous flow domains, are given in terms of streamlines patterns, velocity profiles, pressure contours, and friction coefficient along the impinging wall. The influence of porosity on the flow pattern is shown to be very low in comparison to the effects caused by varying permeability, fluid-layer height, and porous-layer thickness. These finding could be used to advantage when designing engineering equipment, since the use of selected porous materials could reduce undesirable recirculation zones, promote quick flow redistribution, and adjust pressure to required levels.

1. INTRODUCTION

Impinging jets are used in industrial applications mostly as a means of promoting and controlling heat and mass transfer over surfaces. In some instances, one wants to maximize local transfer rates, or, depending on the specific application, a smoother cooling or heating along a surface is desirable. Heat sinks made out of porous metal foams have a wide range of application in maximizing heat transfer to or from surfaces. A good understanding of the flow and pressure fields over a surface covered with some sort of porous material might help engineers in designing more efficient and energy-saving equipment.

The majority of the studies available in the literature refer to heat transfer obtained with a turbulent impinging jet, with some works covering two-dimensional

Address correspondence to Marcelo J. S. de Lemos, Departamento de Energia—IEME, Instituto Tecnológico de Aeronáutica—ITA, 12228-900 São José dos Campos, SP, Brazil. E-mail: delemos@ita.br

NOMENCLATURE

B	jet width	x	direction parallel to the collision plate
c_F	Forchheimer coefficient	x/B	nondimensional longitudinal coordinate
C_f	friction coefficient	y	direction normal to the impinging wall
Da	Darcy number based on channel height $(=K/H^2)$	y/B	nondimensional transverse coordinate
h	porous layer height	ΔP	pressure drop
h_p	nondimensional ratio h/H	ΔP_0	stagnation pressure
H	channel height	μ	dynamic viscosity
K	permeability of the porous medium	ρ	density
L	channel length, $L = 0.3$ m for porous cases, $L = 1.0$ m for clear cases	τ_w	wall shear stress $[=\mu(du/dy)]$
		ϕ	porosity $(=\Delta V_f/\Delta V)$
Re	Reynolds number	ψ_o	rotational intensity
v_{in}	inlet jet velocity	$\langle\rangle^i$	intrinsic average

(2-D) jets in laminar regime. Law and Jacob [1] made an extensive numerical analysis of the hydrodynamic characteristics of a 2-D jet impinging normally against a flat plate. They found differences in the size of the recirculating bubble depending on the length of the confining plates. Baydar [2] measured the hydrodynamic characteristics of single and double jets colliding against a plate. He concluded that a low-pressure region occurs on the impingement plate for Re greater than 2,700, which affects the peaks in heat transfer coefficients. Chen et al. [3] analyzed mass transfer induced by a planar laminar jet and concluded that peak values in Nusselt number occurred at a point ranging from half to one jet width away from the stagnation point. Park et al. [4] compared different numerical methods in simulating the flow filed in such configuration. They showed that their numerical results for laminar jets contained negligible false diffusion.

Several studies investigating thermal and flow characteristics of porous materials have been published in the last few decades. A complete review of the many contributions through the years is beyond the scope of this work, so only a few of them are reviewed here. The thermal performance of porous media was studied by Vafai and Kim [5], who evaluated the heat transfer of a hybrid medium. Huang and Vafai [6] analyzed the heat transfer of a flat plate covered with a porous insert. Effects of the insertion of a porous medium in a flow were presented by Hadim [7], who investigated the flow in a channel, both fully and partially filled with a porous insert. More recently, a number of research papers have been published covering a very wide range of problems involving flow in porous media [8–22], including flows parallel to a layer of porous material [23] and across baffles made of permeable media [24, 25]. Investigation of configurations involving perpendicular jets into a porous core is much needed for optimization of heat sinks attached to solid surfaces. However, studies of porous media under impinging jets are, unfortunately, yet very scarce in the literature.

Examples found are those given by numerical simulations of Kim and Kuznetsov [26], who investigated optimal characteristics of impinging jets into heat sinks, and measurements by Prakash et al. [27, 28], who presented experimental and numerical studies of turbulent jets impinging against a porous layer. Fu et al. [29]

also evaluated the thermal performance of different porous media under an impinging jet.

Motivated by the foregoing application or, say, optimization of thermal sinks modeled as permeable media attached to surfaces, the present work uses the same methodology proposed earlier by Pedras and de Lemos [30, 31], but pays attention now to laminar flows only with the intention to first broaden the knowledge on flow characteristics within such devices. Accordingly, in [30, 31] the authors proposed a macroscopic two-equation turbulence model able to treat calculation domains containing both porous regions and clear (unobstructed) flow passages. Although the development in [30, 31] was initially proposed for the flow variables, it has been extended to nonbuoyant heat transfer in porous media [32]. Further, a consistent program of systematic studies, based on the initial model proposed in [30], for treating buoyant flows [33–37], mass transfer [38], nonequilibrium heat transfer [39, 40] and double diffusion [41], in addition to reviews on macroscopic turbulence modeling [42, 43], have been published. The ability to treat a hybrid (clear/porous) medium, involving transport across a macroscopic interface, has also been investigated [44–46].

Here, a jet flow in laminar regime is considered subjected to variation of several geometric and porous media parameters. This work can be seen as an initial contribution toward a more realistic numerical solution of turbulent heat transfer due to impinging jets on covered surfaces.

2. PHYSICAL MODEL

The physical models evaluated in this work are shown in Figure 1, where a laminar jet impinges normally and freely against a flat plate (Figure 1*a*), or else it crosses through a layer of porous material (Figure 1*b*). For the latter cases, a porous layer of thickness h covers the bottom surface. Thickness of the jet exit nozzle is B and a fully developed laminar flow is assumed at the jet exit. Distance between the jet exit and the lower wall is H. To the left, an ordinary symmetry boundary condition applies. The flow is assumed to be two-dimensional, laminar, and incompressible. Fluid properties are constant, and no buoyancy effects are considered. On the walls, the no-slip condition is used. The channel length is sufficiently long so that fully developed flow is assumed at the channel exit ($x = L$).

3. MATHEMATICAL MODEL

As mentioned, the mathematical model employed here consists of a laminar version of the more complete work presented by Pedras and de Lemos [30, 31]. The jump condition at the macroscopic interface, between the clear region and the porous medium, was considered further in the works of de Lemos [44] and de Lemos and Silva [46]. For the sake of simplicity, however, in this work no jump condition is used. As most of the theoretical development is readily available in the open literature, the governing equations will just be presented; details about their derivations can be obtained in the mentioned works.
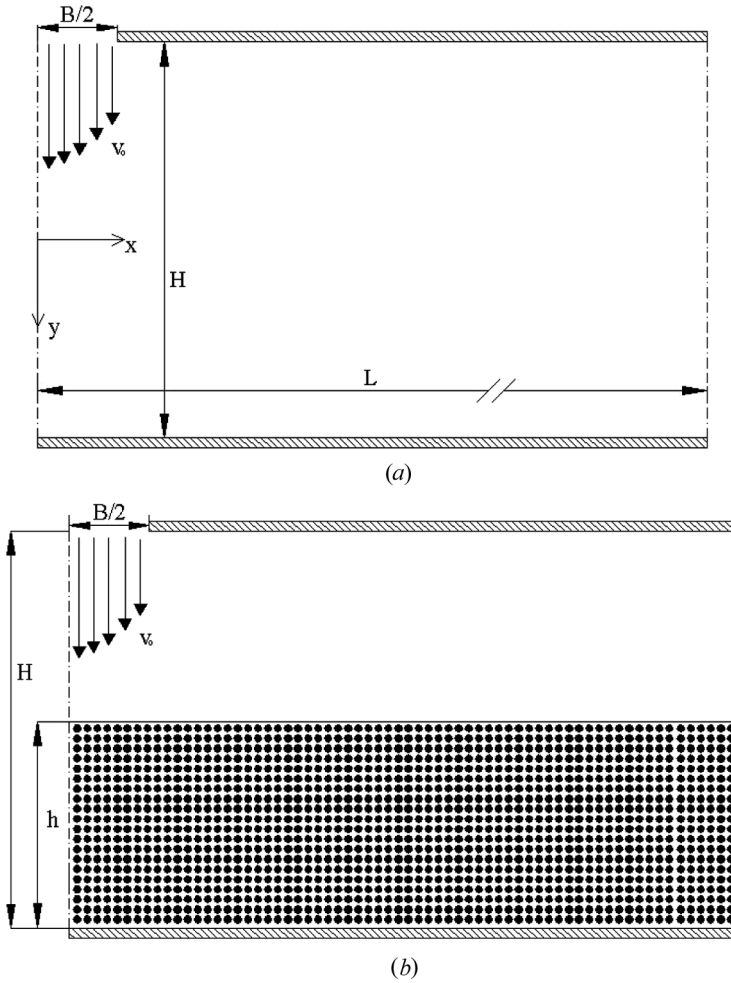
Figure 1. Confined impinging jet: (*a*) clear channel; (*b*) channel with a porous layer of height *h*.

3.1. Macroscopic Continuity Equation

$$\nabla \cdot \mathbf{u}_D = 0 \tag{1}$$

where $\mathbf{u}_D$ is the average surface velocity (also known as Darcy velocity). In Eq. (1) the Dupuit-Forchheimer relationship, $\mathbf{u}_D = \phi\langle\mathbf{u}\rangle^i$, has been used, where ϕ is the porous medium porosity and $\langle\mathbf{u}\rangle^i$ identifies the intrinsic (fluid-phase) average of the local velocity vector $\mathbf{u}$ [47].

3.2. Macroscopic Momentum Equation

$$\rho\nabla \cdot \frac{\mathbf{u}_D\mathbf{u}_D}{\phi} = -\nabla\phi\langle p\rangle^i + \mu\nabla^2\mathbf{u}_D - \left(\frac{\mu\phi}{K}\mathbf{u}_D + \frac{c_F\phi\rho}{\sqrt{K}}|\mathbf{u}_D|\mathbf{u}_D\right) \tag{2}$$

where the last two terms in Eq. (2) represent the Darcy and Forchheimer contributions, respectively. The symbol K is the porous medium permeability, $c_F = 0.55$ is the form drag coefficient (Forchheimer coefficient), $\langle p \rangle^i$ is the intrinsic pressure of the fluid, ρ is the fluid density, and μ represents the fluid viscosity.

At the interface, condition of continuity for velocity and pressure reads

$$\mathbf{u}_D|_{0<\phi<1} = \mathbf{u}_D|_{\phi=1} \tag{3}$$

$$\langle p \rangle^i|_{0<\phi<1} = \langle p \rangle^i|_{\phi=1} \tag{4}$$

The nonslip condition for velocity is applied on both walls.

3.3. Numerical Method

The numerical method utilized to solve the flow equations is the finite-volume method applied to a boundary-fitted coordinate system. Equations (1) and (2), subjected to boundary and interface conditions given by Eqs. (3) and (4), were discretized in a 2-D control volume involving both clear and porous media. The numerical method used in the resolution of the equations above was the SIMPLE algorithm, described by Patankar [48]. The interface is positioned to coincide with the border between two control volumes, generating only volumes of the types "totally porous" or "totally clear". The flow equations are then resolved in the porous and clear domains, considering the interface conditions mentioned earlier. Details of the numerical implementation can be seen in Pedras and de Lemos [30, 31].

4. RESULTS AND DISCUSSION

4.1. Mesh Independence and Code Validation

Mesh dependence studies were conducted for several grids, spanning from a small 40×200 grid to a more refined 160×200 mesh. A typical grid with nodes concentrated at the wall is presented in Figure 2a. Difference in calculating the friction coefficient C_f using all grids was less than 0.5%. Results for C_f along the impingement wall and close to the stagnation point are presented in Figure 2b using distinct grids. Because of the intense velocity gradients within that region, friction factor determination tends to be harder therein and the influence of the mesh size on the results turns out to be more sensitive around $x/B = 0$. Inspecting the figure, one can see that for grids above 80×200, no detectable difference was observed on calculated C_f. Therefore, all results herein were obtained using 16,000 nodal points, for both clear-channel and porous-medium runs.

For numerical code validation, friction coefficients calculated along the impingement plate for unobstructed channel (clear medium) were compared with available data in the literature. Comparisons were also made for C_f calculated at distances far away from the stagnation point (right exit on Figure 1a). After the stagnation region, where the velocity gradients are high and friction coefficient shows intense variation, the flow tends toward a fully developed laminar profile in a 2-D channel, for which an exact solution is available.
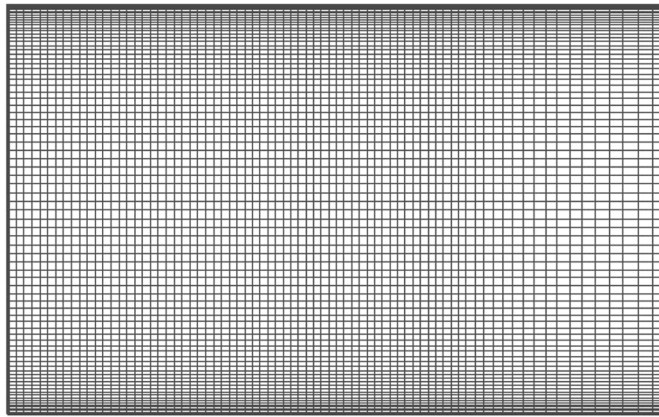
(*a*)
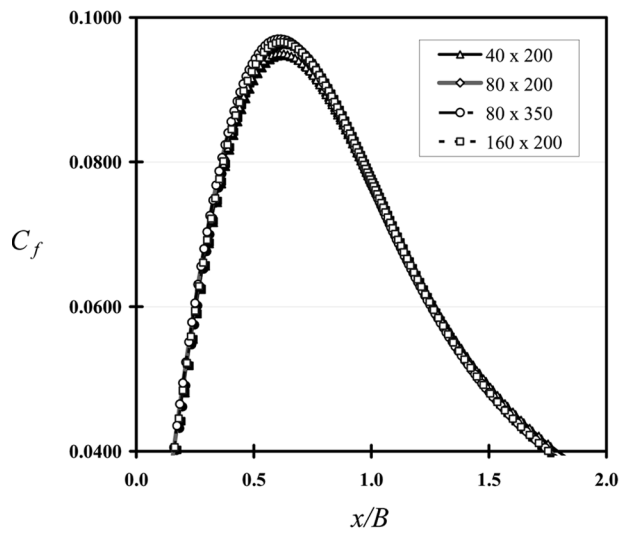
(*b*)

Figure 2. Grid independence studies: (*a*) typical mesh with node concentration closed to both walls; (*b*) variation of C_f along the bottom plate for $H/B = 2$, Re = 1,000.

The friction factor along the impingement plate is defined as

$$C_f = \frac{\tau_w}{1/2\ \rho v_{\text{in}}^2} \tag{5}$$

For fully developed flow in a 2-D channel, Figure 3*a* shows friction coefficient calculated by the exact solution given by Law et al. [1],
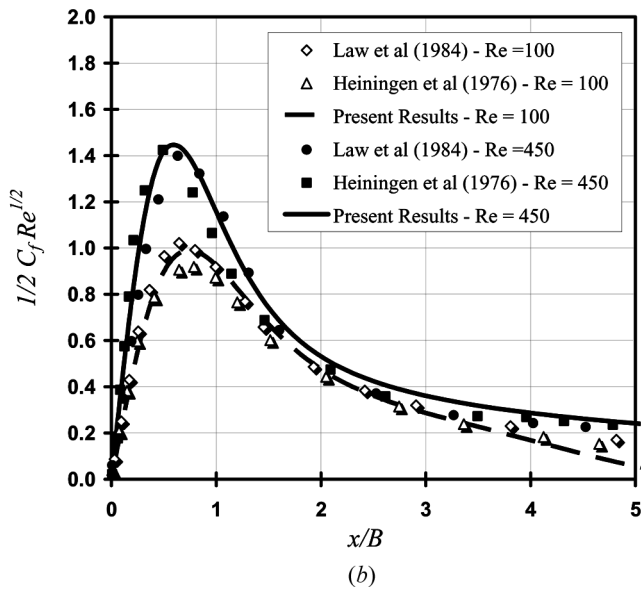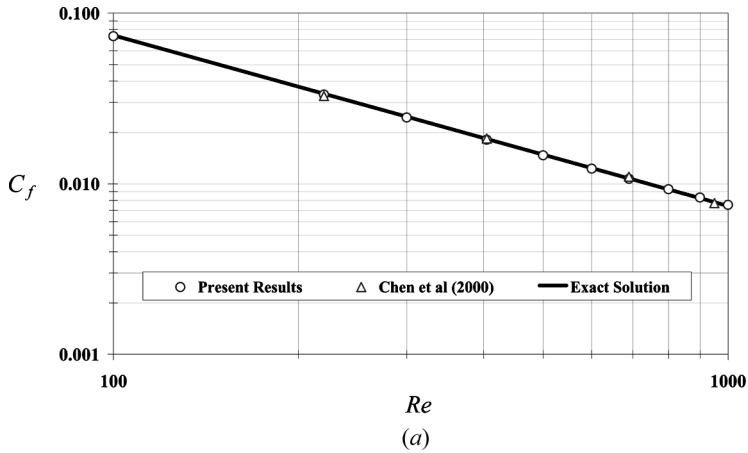
$$C_f = \frac{6}{\text{Re}(H/B)^2} \tag{6}$$

Figure 3. Comparison of calculated friction factor C_f with literature results: (*a*) fully developed flow with $H/B = 0.9$ and $L/H = 111$; (*b*) friction coefficient near the stagnation point.

Also shown in the figure are computations by Chen et al. [3] in addition to the present results. Maximum relative error between exact and numerical solution was less than 1.5%. For this case, on $L = 1.0$-m-long channel was used, giving $L/H = 111$ to guarantee fully developed flow at exit, even though a 0.3-m length was enough for fully developed flow to be established. Figure 3*b* shows a comparison between numerical simulations and literature results [1, 49] for the friction coefficient variation along the impingement wall. As can be seen, values rise quickly from zero at the symmetry region to a maximum value close to the stagnation point, decreasing afterwards until the flow turns into a completely developed one and the friction coefficient reaches a constant value. The peak of C_f close to the stagnation region
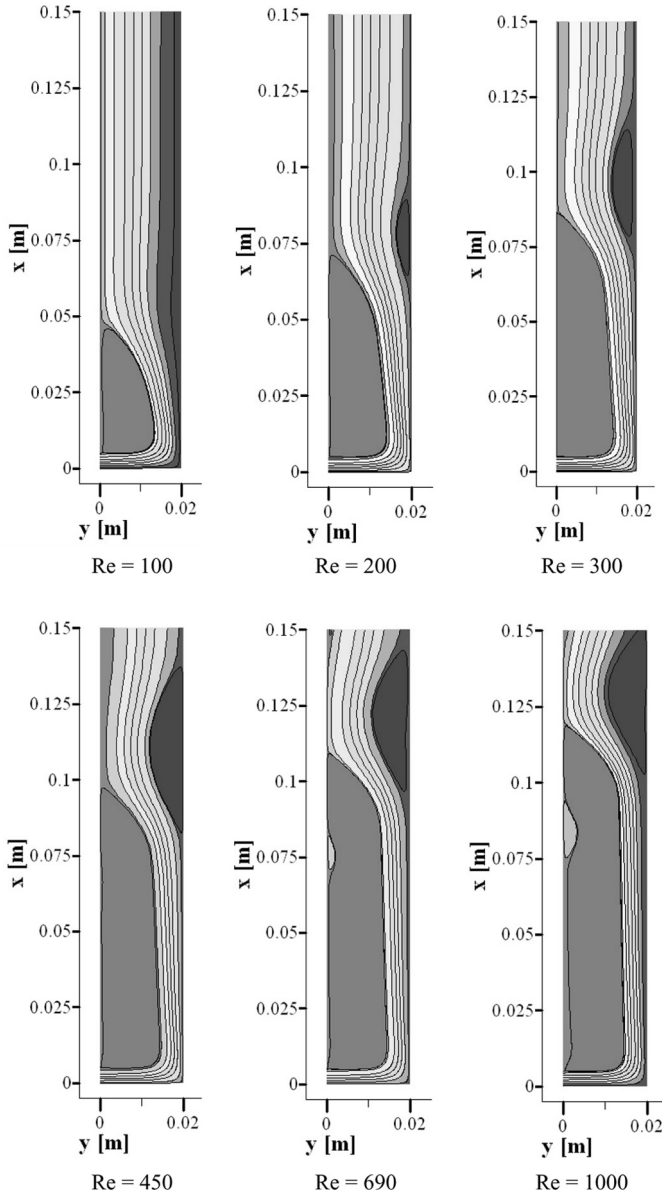
Figure 4. Effect of Re on streamlines for clear channel, $H/B = 2$.

Table 1 Effect of Re on rotational intensity Ψ_0 for $H/B = 2$

	Rotational intensity (Ψ_0)					
	Re = 100	Re = 200	Re = 300	Re = 450	Re = 690	Re = 1,000
Primary	0.212	0.233	0.265	0.304	0.330	0.360
Secondary	0.000	0.006	0.036	0.090	0.154	0.195

comes from the intense deceleration of the impinging fluid, resulting in high wall shear stress in this region.

4.2. Clear Channel

First, this section presents simulations of the flow and pressure fields for a confined jet impinging onto the bottom surface of Figure 1a. The channel is empty and
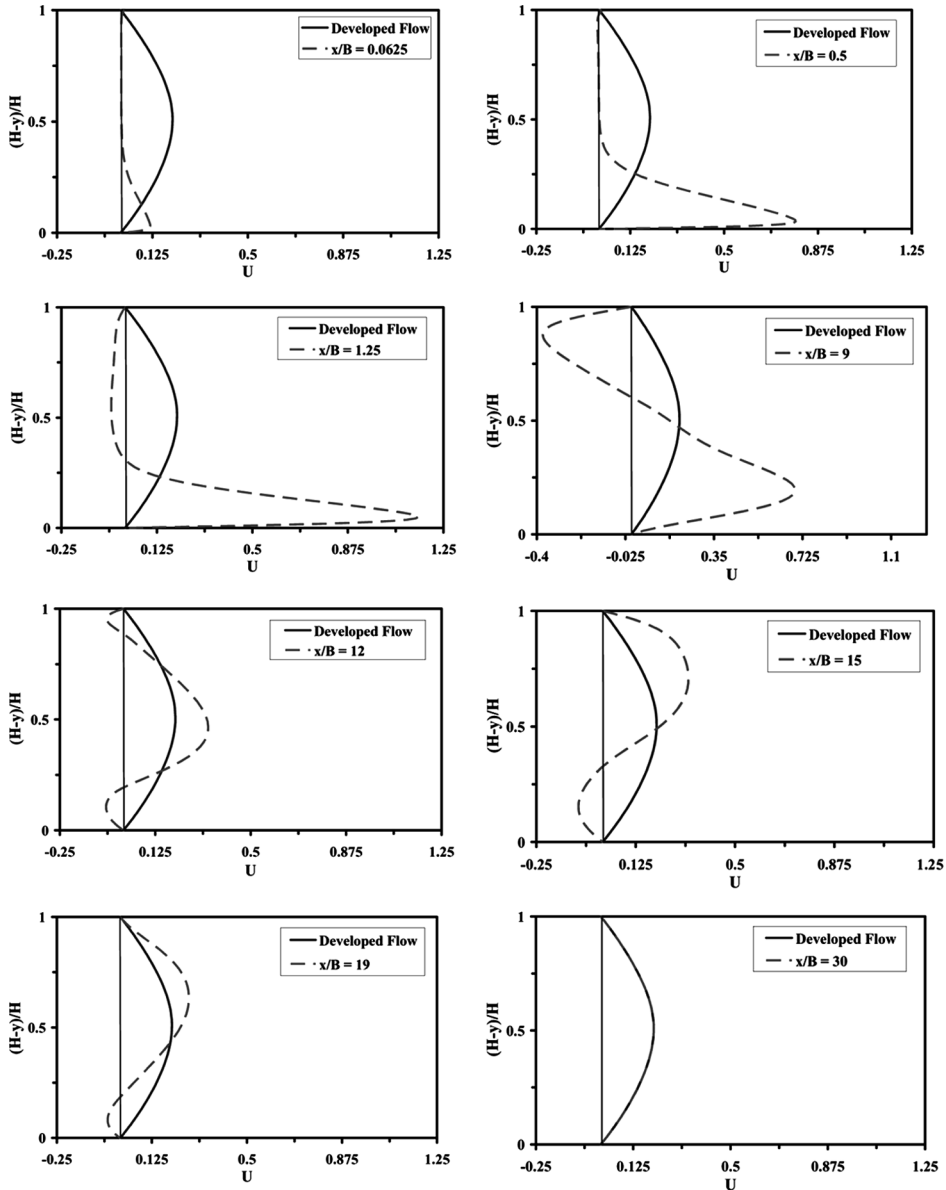

Figure 5. Streamwise velocity profiles for clear channel, $H/B = 4$, Re = 200.

the flow leaves to the right and left, reaching a fully developed condition far away from the stagnation region. The effect of Reynolds number on the confined flow field can be investigated qualitatively by observing the streamline contours. Figure 4 shows the streamlines for $H/B = 2$ for different Re. For this situation, the flow is dominated by the presence of a primary and a secondary vortex. The figure indicates that the secondary vortex is much smaller and weaker than the first one in terms of rotational intensity ψ_0, which has been defined by Kelkar and Patankar [50] as the ratio of vortex mass flow rate to the overall mass flow rate. Rotational intensities are presented in Table 1. The second vortex appears for Re above 200, and a third recirculation is observed attached to the upper wall (shown at the left in Figure 4), at about $x/B = 8$ ($x = 0.08$ m) and connected to the primary vortex for Re = 690, even though its rotational intensity is almost negligible. It is also seen that both primary and secondary recirculations grow quickly for Re up to 450, remaining thereafter at about the same size for Re up to 1,000. Recirculating zones are also clearly observed in Figure 5, which shows velocity profiles for $H/B = 4$ and Re = 200. Negative values for the velocity profile indicate back flow and the presence of recirculation zones. Fully developed condition is achieved for $x/B = 30$. The graph for $x/B = 9$ is represented in a different scale in order to accommodate all the negative values of the computed velocity.

Figure 6 further shows the vortex center for both primary and secondary vortices. It is noticeable that the center of vortices moves downstream with increasing Reynolds number. Such movement seems to occur at a faster pace for lower values of Re. Figure 6 suggests that the vortex position stabilizes after a certain Re for each H/B ratio. Unfortunately, because of the few cases run, one can only speculate about a possible dependence of the stabilization position with Re and H/B.

Pressure distribution along the bottom plate is discussed next. Figure 7a shows the nondimensional pressure at the bottom surface, close to the stagnation region
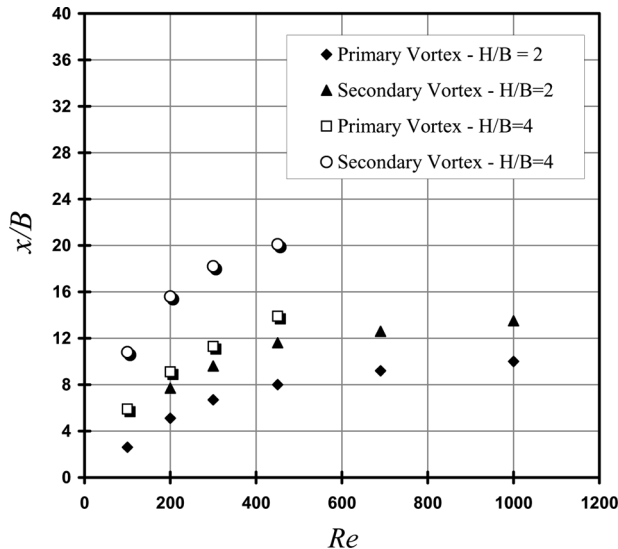

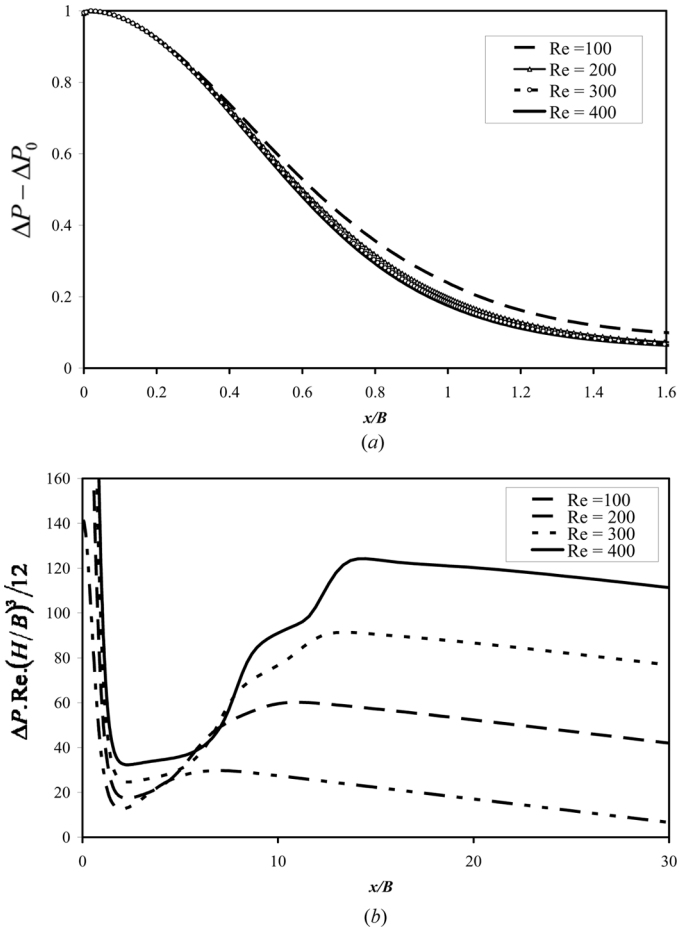**Figure 6.** Variation of vortex center position with Re for clear channel.

Figure 7. Effect of Re on local pressure along the impingement surface, $H/B = 2$: (*a*) near the stagnation flow region, $x/B < 1.6$; (*b*) along the entire plate.

and for $H/B = 2$. Maximum local pressure occurs at the stagnation region, decreasing from its maximum value afterwards. Values for the stagnation pressure ΔP_0 are shown in Table 2 for $H/B = 2$, where it can be seen that ΔP_0 increases with Reynolds number. Figure 7*b* shows pressure distribution along the bottom wall. For a fully developed flow in a parallel-plate channel, the pressure gradient along the channel

Table 2. Stagnation pressures ΔP_0 for $H/B = 2$

Re	Present results	Law et al.
100	2.12	1.938
200	2.22	2.085
300	2.25	2.137
400	2.26	2.164

can be evaluated as proposed by Law et al. [1], in the form

$$\left(\frac{dP}{dx}\right)\bigg|_{y=H} = -\frac{12}{\mathrm{Re}(H/B)^3} \tag{7}$$

Pressure is plotted in terms of the nondimensional parameter $\Delta P \cdot \mathrm{Re} \cdot (H/B)^3/12$, so that for a fully developed condition the slope of such curves tends to -1. The figure indicates clearly the point where the flow becomes fully developed and the curves turn into straight lines.

4.3. Porous Layer

The results that follow consider a porous layer attached to the impinging wall at the bottom (see Figure 1b). The default parameters used in the simulations are $\mathrm{Re} = 1{,}000$, $H/B = 2$, $\mathrm{Da} = K/H^2 = 8.28 \times 10^{-3}$ $(K = 3.31 \times 10^{-6}\,\mathrm{m}^2)$, $\phi = 0.9$, and $h_p = 0.50$. For such porous media runs, these parameters were varied in order to assess their effect on the flow field. Table 3 lists the values used for all cases presented.

4.3.1. Effect of Re. Figure 8 shows the streamlines for several Re, keeping all other parameters constant. With the addition of the porous layer, the secondary recirculation, previously observed in the clear-medium section (see Figure 4), completely vanishes and the primary recirculating bubble is significantly decreased in size and in rotational intensity. Reduction of ψ_0 can be better seen when comparing

Table 3. Data for cases considering a porous layer over the impinging wall

| Parameter	Re	H/B	h_p	ϕ	K (m²)	$\mathrm{Da} = K/H^2$	$\psi_{0,\mathrm{primary}}$	$\psi_{0,\mathrm{secondary}}$
Re	100	2	0.50	0.9	3.31E-06	8.28E-03	0.074	0
	200						0.086	0
	300						0.092	0
	400						0.096	0
	500						0.100	0
	1,000						0.111	0
H/B	1,000	0.9	0.50	0.9	3.31E-06	4.09E-02	0.011	0
		2				8.28E-03	0.111	0
		4				2.07E-03	0.264	0
h_p	1,000	2	0.25	0.9	3.31E-06	8.28E-03	0.180	0.02
			0.50				0.110	0
			0.75				0.036	0
ϕ	1,000	2	0.50	0.5	3.31E-06	8.28E-03	0.110	0
				0.7			0.120	0
				0.9			0.110	0
$\mathrm{Da} = K/H^2$	1,000	2	0.50	0.9	2.70E-04	6.75E-01	0.112	0
					1.36E-05	3.40E-02	0.111	0
					3.31E-06	8.28E-03	0.110	0
					1.03E-07	2.58E-04	0.078	0
					1.80E-08	4.50E-05	0.065	0
					5.36E-09	1.34E-05	0.052	0
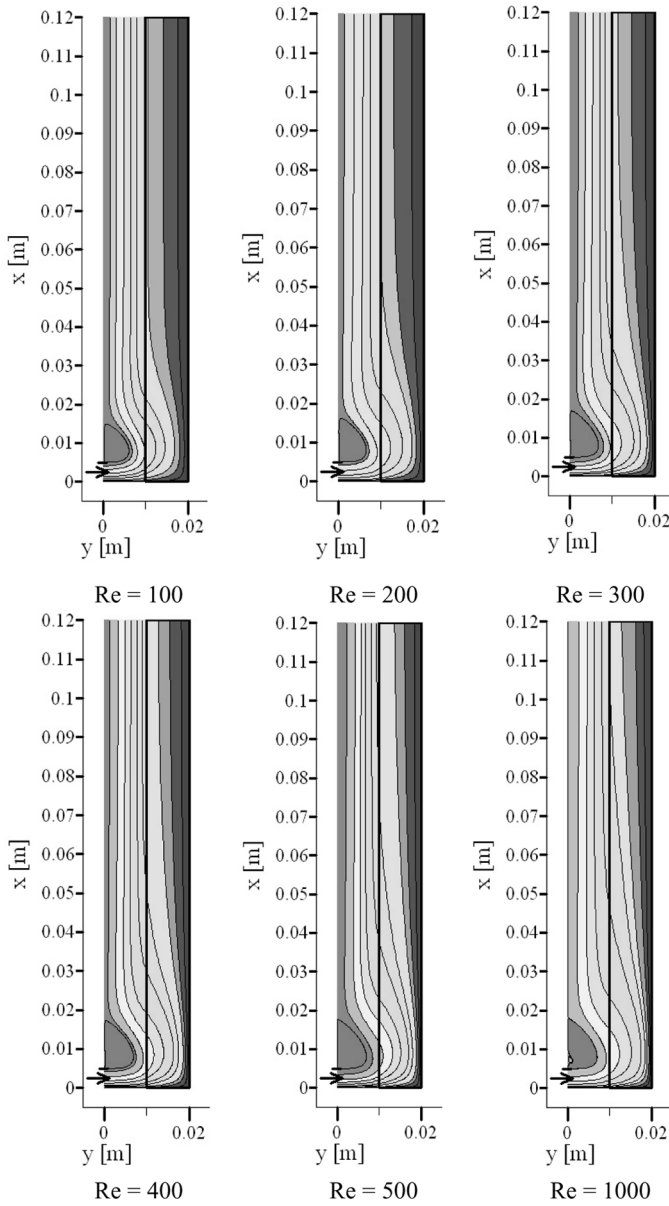
Figure 8. Streamlines for $h_p = 0.50$, $Da = 8.28 \times 10^{-3}$, $\phi = 0.9$, $H/B = 2$, $L/H = 15$.

corresponding numbers in Tables 1 and 3. Also indicated in Figure 8 is that, regardless of Re, the location of the primary recirculation stays fixed, a feature that could be used to some advantage when designing systems involving heating or cooling jets.

Corresponding values for C_f, restricted to the stagnation region, are further presented in Figure 9. Within that region, the friction coefficient shows intense
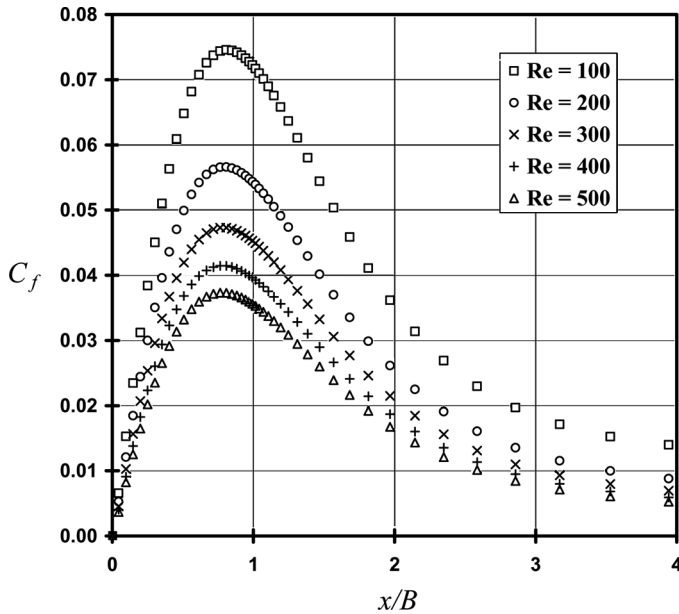
Figure 9. Variation of C_f along the impingement plate for $H/B = 2$, $h_p = 0.50$, $\phi = 0.9$, $Da = 8.28 \times 10^{-3}$, $L/H = 15$.

variation, with the peak values located before $x/B = 1$. It can be noticed that C_f results decrease with increasing Re, for both the stagnation and developed flow regions ($x/B > 4$). This behavior can be explained if one inspects Eq. (5), since an increase in the velocity of the incoming jet decreases C_f at a faster rate than the increase in τ_w at the wall. This happens because the decrease of C_f due to the inlet velocity is proportional to v_{in}^2, whereas an increase in τ_w varies linearly with the velocity u close to the wall.

4.3.2. Effect of H/B. The effect of the geometric parameter H/B is presented in Figure 10, where the streamlines along the channel are shown. With increase in the channel height H, while keeping the same mass flow rate through the jet, the primary recirculation grows in size and intensity, as can be seen in Table 3. Small-size passages tend to channel the flow, whereas large void spaces give rise to recirculating flow motions. These results are interesting because one knows that an increase in ψ_0 indicates that more incoming flow kinetic energy is being wasted to drive larger recirculation bubbles.

Figure 11 shows the C_f variation close to the stagnation region for three values of H/B. From the figure, two interesting points can be observed, the first being the decrease in C_f as H/B increases and the second the displacement of the C_f peak value along the x/B coordinate. The first one, the reduction of C_f, is a consequence of the fact that the porous substrate acts as an obstacle and a flow distributor, so that the jet spreads faster and the wall shear stress close to the stagnation drops. The second observation, the right movement of the peak value, can be explained using similar arguments. Keeping the same mass flow rate through the jet while increasing the size
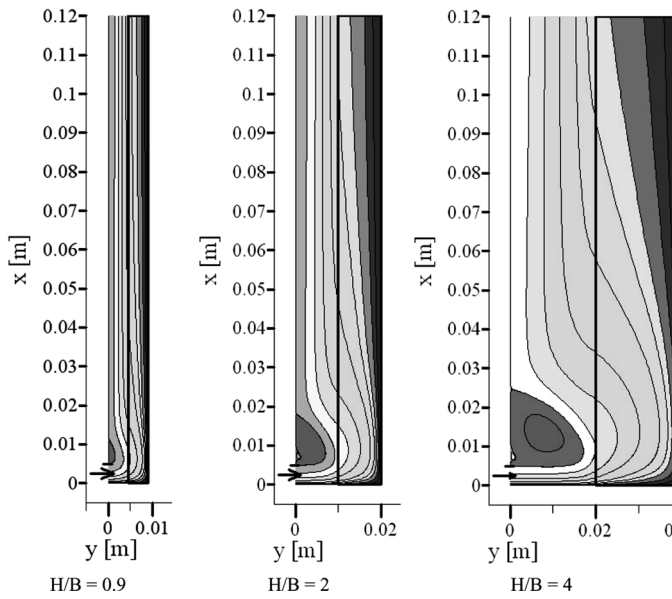
Figure 10. Streamlines for $Re = 1,000$, $h_p = 0.50$, $\phi = 0.9$, $Da = 8.28 \times 10^{-3}$, $L/H = 15$.

of the porous matrix make velocity gradients within the porous material less intense, so that the flow changes its direction earlier and more gradually as it approaches the bottom wall. The streamwise position at the wall, where the streamlines are more concentrated, is displaced farther to the right. Consequently, the largest velocity
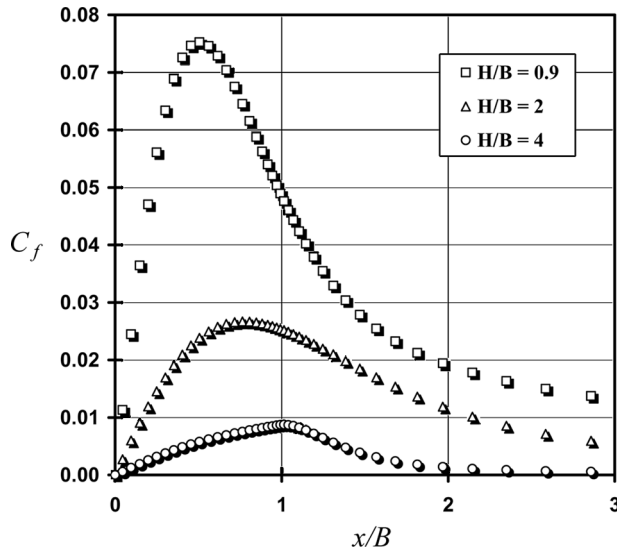

Figure 11. Variation of C_f along the impingement wall for $Re = 1,000$, $h_p = 0.50$, $\phi = 0.9$, $Da = 8.28 \times 10^{-3}$, $L/H = 15$.

gradients at the wall are moved downstream, causing the peak in C_f, due to the highest value of τ_w, to appear farther to the right.

4.3.3. Effect of h_p. Figure 12*a* shows streamfunction contours for a porous layer of distinct heights, keeping all other parameters constant. For $h_p = 0.25$, a secondary recirculation bubble appears close to the wall, around the porous/clear
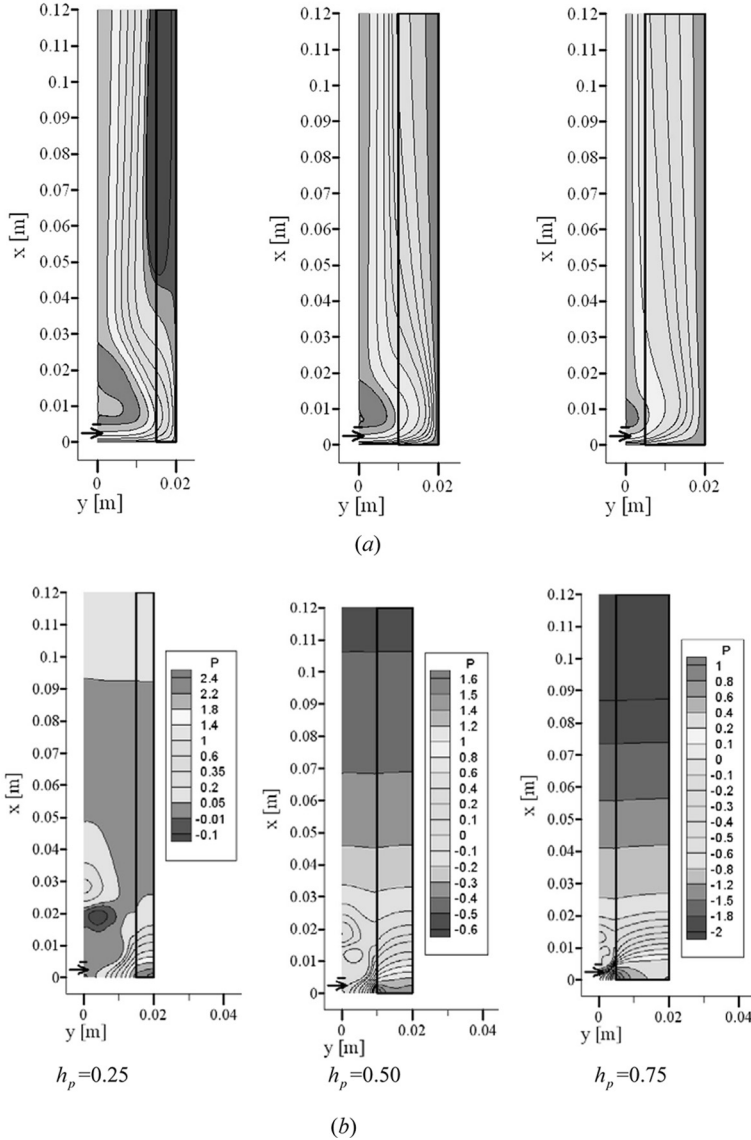

Figure 12. Effect of h_p on streamlines (*b*) and pressure contours (*b*) for Re = 1,000, $\phi = 0.9$, Da = 8.28×10^{-3}, $H/B = 2$, $L/H = 15$.

media interface and farther downstream. This secondary recirculating flow is of considerable size and intensity, as can be seen in Table 3. A third one can still be observed upstream (not shown in the figure), though its intensity is almost negligible. For $h_p = 0.50$, the upstream vortex is reduced to about 40% of its intensity and the secondary one essentially disappears. For $h_p = 0.75$, the primary recirculation decreases considerably in size, with its intensity reaching 20% of the value for $h_p = 0.25$ and only 10% if one compares it with the clear-channel case shown in Table 1.

Figure 12b shows the influence of h_p in the pressure contours along the channel. The contour levels are at different scales in order to better show the pressure behavior. For $h_p = 0.25$, the highest pressure levels reaches $2.4\,\text{N/m}^2$ at the stagnation point. With an increase in h_p, this level decreases, reaching $1.6\,\text{N/m}^2$ for $h_p = 0.50$ and $1.0\,\text{N/m}^2$ for $h_p = 0.75$. Because of the flow redistribution obtained when a fluid permeates though a porous matrix, flow development occurs earlier, as can also be seen by looking at the constant pressure levels, which tend to become straight lines early for higher values of h_p. Also, one can note a displacement of the highest pressure point, along the y axis, which appears to move toward the interface region for higher values of h_p.

Corresponding values for the friction coefficient C_f are presented in Figure 13 and show its variation along the impingement plate. With an increase in h_p, the peak value of C_f drops. This happens because the porous layer acts as an obstacle to the impinging jet, distributing the flow more evenly and reducing the velocity gradients in the stagnation region. However, moving downstream in the flow toward a fully developed condition, the friction coefficient drops more intensely for lower values
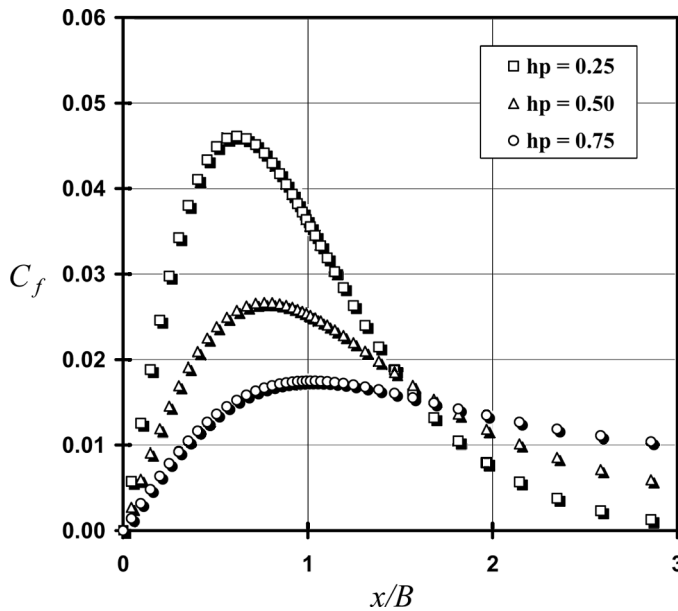

Figure 13. Variation of C_f along the impinging wall for $\text{Re} = 1{,}000$, $\phi = 0.9$, $\text{Da} = 8.28 \times 10^{-3}$, $H/B = 2$, $L/H = 15$.
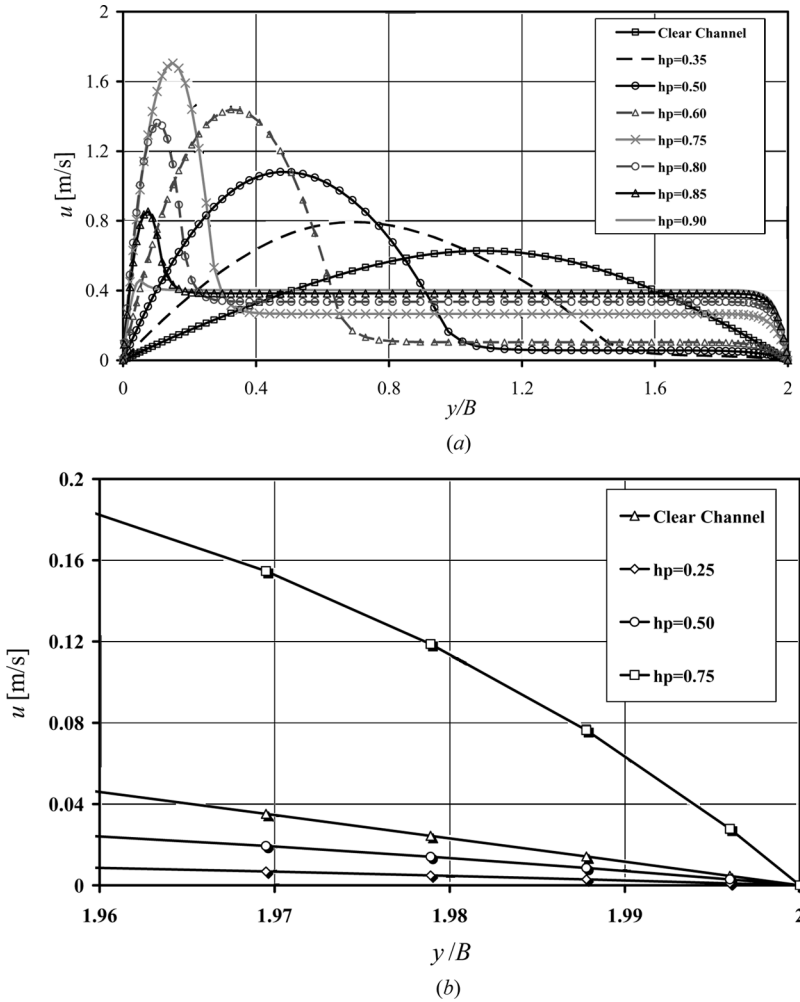
Figure 14. Velocity profiles at channel exit for $Re = 1,000$, $\phi = 0.9$, $Da = 8.28 \times 10^{-3}$, $H/B = 2$, $L/H = 15$: (*a*) entire channel; (*b*) close-up view near the wall.

of h_p, so that an inversion in the former behavior occurs, i.e., the flow with higher h_p results in greater fully developed C_f values. This can be explained with the help of Figure 14*a*, which shows the fully developed velocity profiles at the exit of the

Table 4. Fully developed friction coefficient for different values of h_p; $Re = 1,000$, $\phi = 0.9$, $Da = 8.28 \times 10^{-3}$, $H/B = 2$, $L/H = 15$

	Fully developed friction coefficient			
	Clear channel	$h_p = 0.25$	$h_p = 0.50$	$h_p = 0.75$
C_f	0.0015	0.0003	0.0010	0.0042

channel. With an increase in the height of the porous layer, the velocity profile inside the porous medium tends to become more homogeneous, while the velocity of the clear medium rises due to mass conservation. Looking at Figure 14b, which presents the velocity profiles close to the bottom wall, it can be seen that the velocity gradients close to the wall are higher for higher values of h_p. One can then conclude that for the fully developed condition, friction coefficient increases with an increment in h_p, as indicated by Table 4.

4.3.4. Effect of ϕ. The effect of the porosity is presented in Figure 15, which shows ϕ effects on the streamlines (a) and on the pressure contours (b) along the
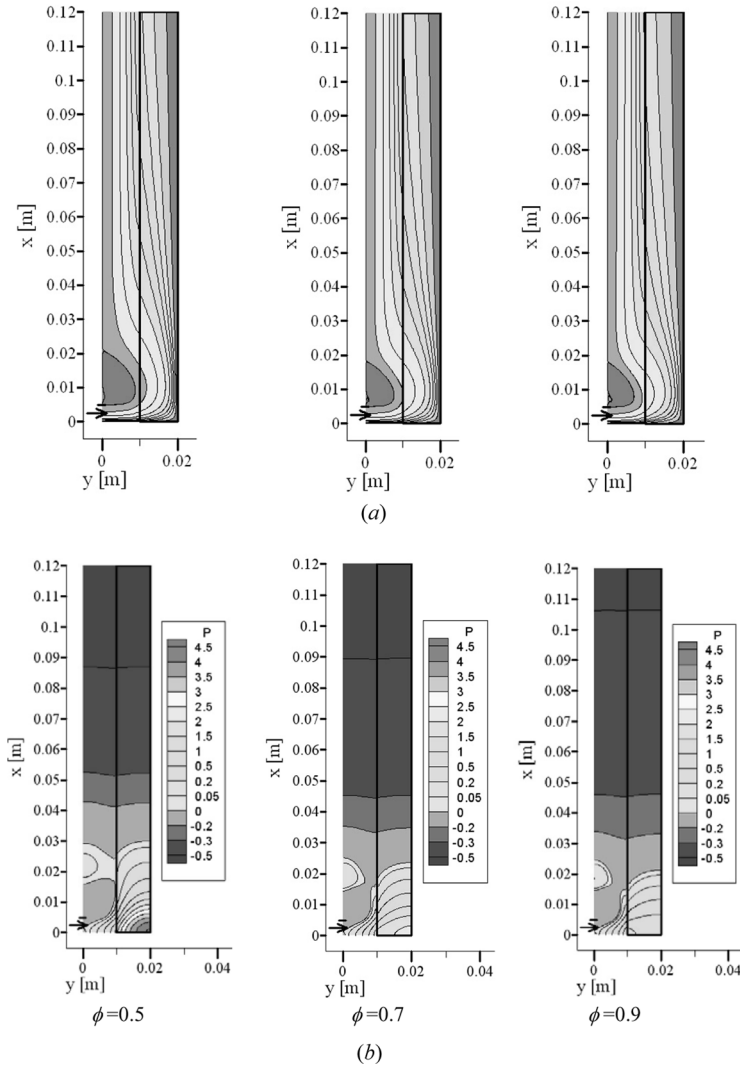

(a)

(b)

Figure 15. Effect of porosity ϕ on streamlines (a) and pressure fields (b) for Re $= 1{,}000$, $H/B = 2$, $L/H = 15$, $h_p = 0.50$, Da $= 8.28 \times 10^{-3}$.
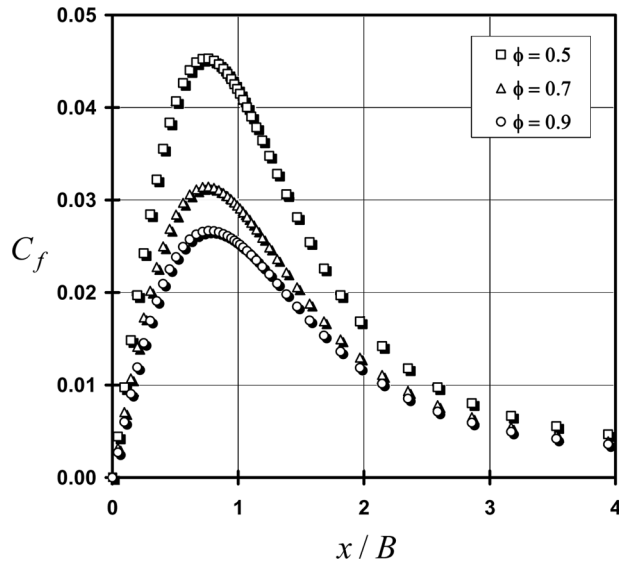
Figure 16. Variation of C_f along the impingement wall $Re = 1,000$, $H/B = 2$, $L/H = 15$, $h_p = 0.50$, $Da = 8.28 \times 10^{-3}$.

channel. Looking at the figures, it can be seen that the porosity does not have a significant influence on the flow pattern. The size and intensity of the primary recirculation also does not reflect a great change, as can be observed in Table 3.

Figure 16 gives the friction coefficient along the impingement plate. It can be seen that the value of C_f at the stagnation region decreases with an increase in
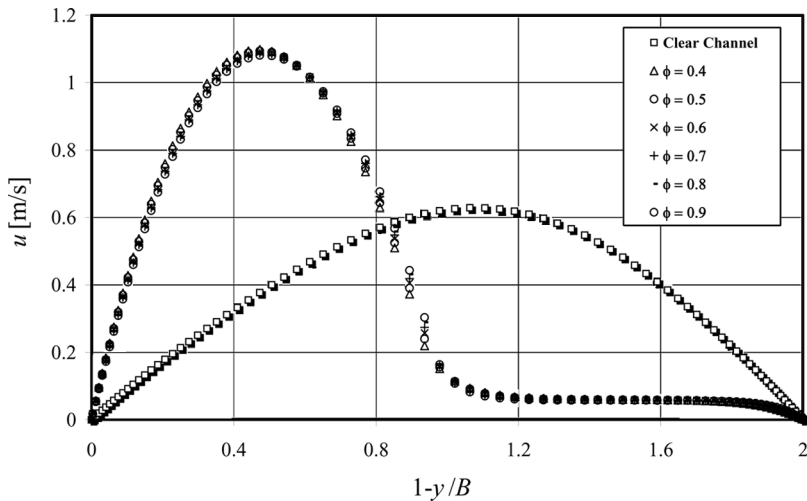

Figure 17. Velocity profiles at channel exit for $Re = 1,000$, $H/B = 2$, $L/H = 15$, $h_p = 0.50$, $Da = 8.28 \times 10^{-3}$.

porosity, though its influence is very small in the developed region. Figure 17 shows the fully developed velocity profiles at the channel exit, giving evidence once again that the porosity does not play a significant role in the flow behavior.

4.3.5. Effect of Da. Figure 18 shows the influence of Da on the streamlines. From the figure, it is easy to see that Da has a great influence on the flow pattern, with an intense decrease in the primary recirculation size and intensity, as can be
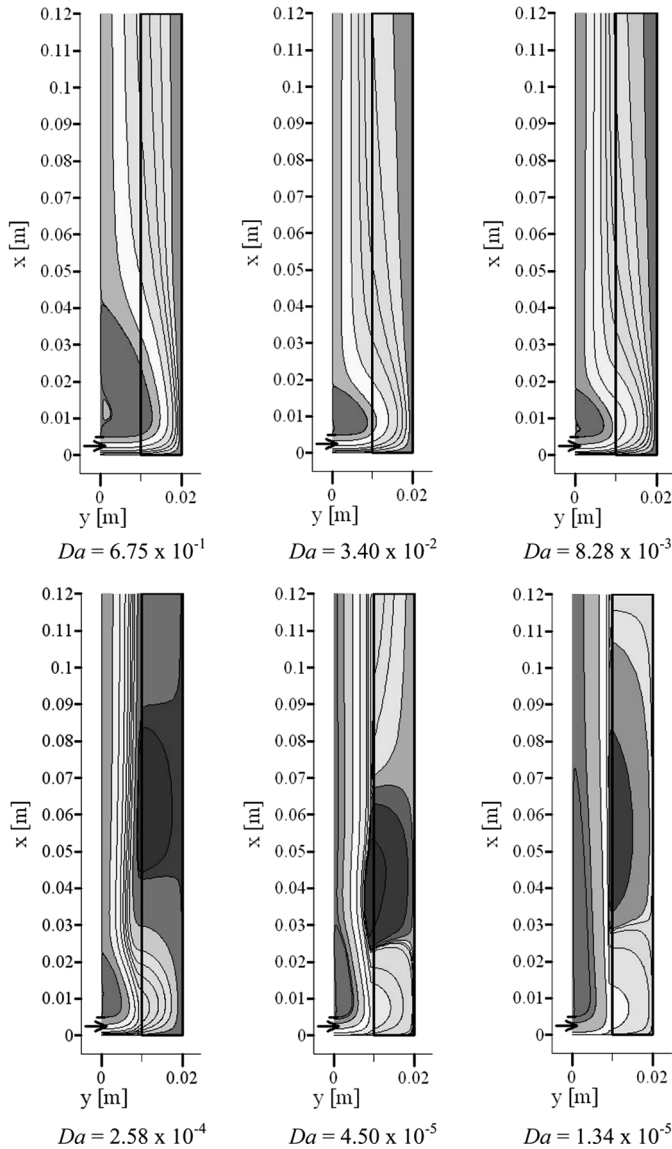
Figure 18. Effect of Da on streamlines for Re = 1,000, $H/B = 2$, $L/H = 15$, $h_p = 0.50$, $\phi = 0.9$.
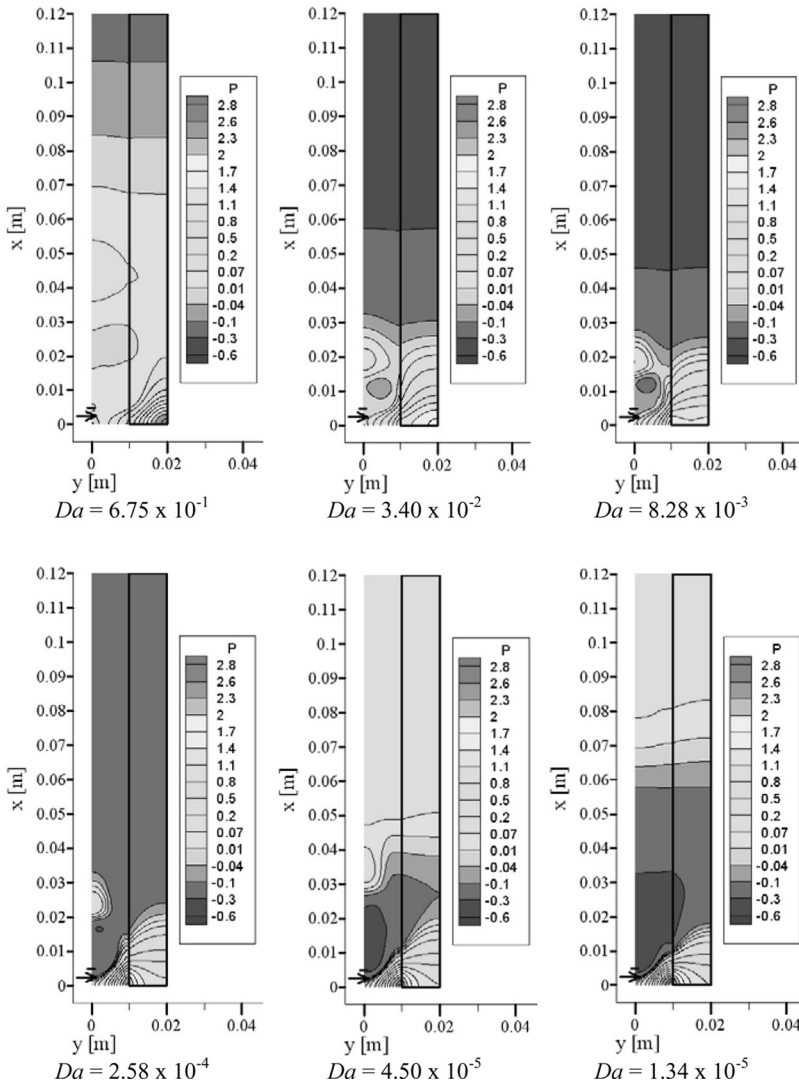
Figure 19. Effect of Da on pressure field for Re = 1,000, $H/B = 2$, $L/H = 15$, $h_p = 0.50$, $\phi = 0.9$.

confirmed by Table 3. For $Da = 2.58 \times 10^{-4}$ and less, a secondary recirculation seems to appear farther along the upstream flow, but its intensity is negligible. For values of Da less than 8.28×10^{-3}, penetration of fluid inside the porous substrate becomes very difficult, and the flow tends to develop almost entirely within the clear region.

From the pressure contours in Figure 19, the effect of the permeability on the flow pattern can be observed clearly. With a decrease of the permeability or Da, the point with the highest static pressure tends to move along the y/B axis toward the interface. Since by decreasing Da one gets a less permeable porous matrix, harder to penetrate, its behavior resembles that of a solid wall. Therefore, higher pressures
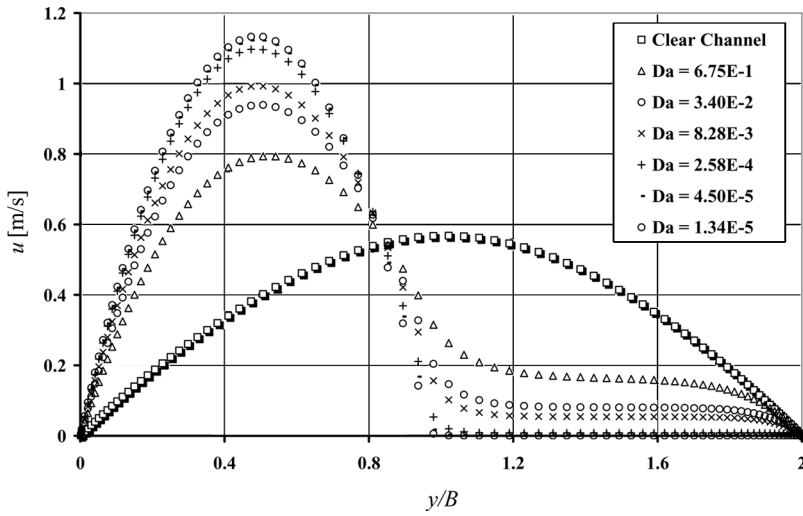
Figure 20. Velocity profiles at channel exit for Re = 1,000, $H/B = 2$, $L/H = 15$, $h_p = 0.50$, $\phi = 0.9$.

tend to move toward the interface, as in the case of a jet impinging on a regular surface.

Figure 20 shows fully developed velocity profiles at the channel exit. As expected, with a lower permeability, penetration of the flow into the porous medium
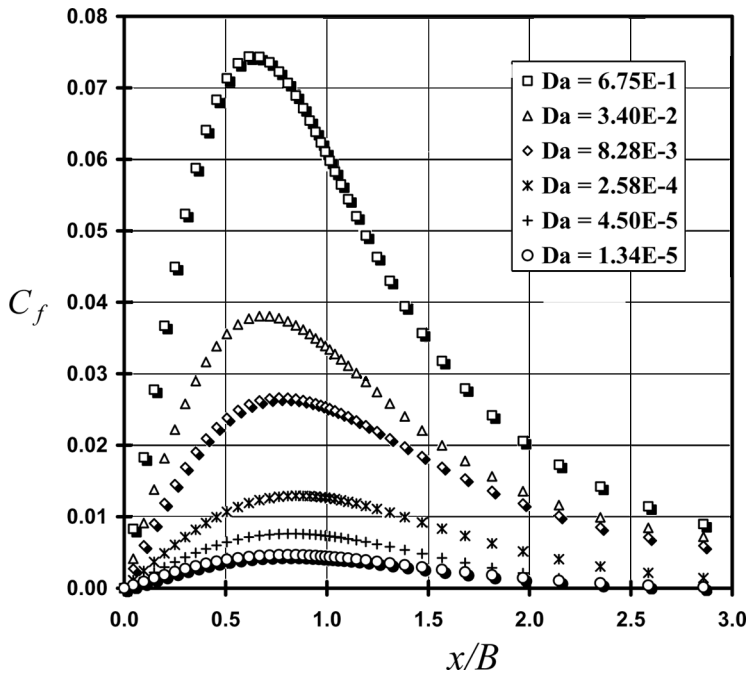

Figure 21. Effect of Da on C_f for Re = 1,000, $H/B = 2$, $L/H = 15$, $h_p = 0.50$, $\phi = 0.9$.

becomes more difficult, resulting in lower velocities inside the porous layer and higher velocities in the clear-medium region. Figure 21, finally, shows the friction coefficient variation along the impingement wall. As can be seen, with an increase in Da, C_f value increases. The increase in the permeability results in easier penetration of the fluid into the porous substrate, so that the impinging jet reaches the collision plate with greater velocity. This generates a higher velocity gradient in the stagnation region, which, in turn, results in higher values of C_f.

5. CONCLUDING REMARKS

For confined laminar impinging jets, it can be concluded that the addition of a porous layer covering the collision surface contributes to a reduction of the amount of recirculating flow, as the flow become more evenly distributed as it passes through the porous material. The influence of porosity on the flow pattern has been shown to be very low in comparison to the permeability (Da), fluid-layer height (H/B), and porous-layer thickness (h_p) effects.

These findings could be used to advantage when designing engineering equipment. The use of selected porous materials, in terms of their properties and geometric parameters, could reduce undesirable recirculation zones, promote quick flow redistribution, and adjust pressure to required levels.

REFERENCES

1. H. S. Law and H. M. Jacob, Numerical Prediction of the Flow Field due to a Confined Laminar Two-Dimensional Submerged Jet, *Comput. Fluids*, vol. 12, pp. 199–215, 1984.
2. E. Baydar, Confined Impinging Air Jet at Low Reynolds Numbers, *Exp. Thermal Fluid Sci.*, vol. 19, pp. 27–33, 1999.
3. M. Chen, R. Chalupa, A. C. West, and V. Modi, High Schmidt Mass Transfer in a Laminar Impinging Slot Jet, *Int. J. Heat Mass Transfer*, vol. 43, pp. 3907–3915, 2000.
4. T. H. Park, H. G. Choi, J. Y. Yoo, and S. J. Kim, Streamline Upwind Numerical Simulation of Two-Dimensional Confined Impinging Slot Jets, *Int. J. Heat Mass Transfer*, vol. 46, pp. 251–262, 2003.
5. K. Vafai and S. J. Kim, Analysis of Surface Enhancement by a Porous Substrate, *J. Heat Transfer*, vol. 112, pp. 700–706, 1990.
6. P. C. Huang and K. Vafai, Flow and Heat Transfer Control over an External Surface Using a Porous Block Array Arrangement, *Int. J. Heat Mass Transfer*, vol. 36, pp. 4019–4032, 1993.
7. A. Hadim, Forced Convection in a Porous Channel with Localized Heat Sources, *J. Heat Transfer*, vol. 116, pp. 465–472, 1994.
8. Y. Zhang, X. F. Peng, and I. Conte, Heat and Mass Transfer with Condensation in Non-saturated Porous Media, *Numer. Heat Transfer A*, vol. 52, pp. 1081–1100, 2007.
9. M. E. Taskin, A. G. Dixon, and E. H. Stitt, CFD Study of Fluid Flow and Heat Transfer in a Fixed Bed of Cylinders, *Numer. Heat Transfer A*, vol. 52, pp. 203–218, 2007.
10. T. Basak, S. Roy, and H. S. Takhar, Effects of Nonuniformly Heated Wall(s) on a Natural-Convection Flow in a Square Cavity Filled with a Porous Medium, *Numer. Heat Transfer A*, vol. 51, pp. 959–978, 2007.

11. V. Bubnovich, L. Henriquez, and N. Gnesdilov, Numerical Study of the Effect of the Diameter of Alumina Balls on Flame Stabilization in a Porous-Medium Burner, *Numer. Heat Transfer A*, vol. 52, pp. 275–295, 2007.

12. X. B. Chen, P. Yu, S. H. Winoto, and H. T. Low, Free Convection in a Porous Wavy Cavity Based on the Darcy-Brinkman-Forchheimer Extended Model, *Numer. Heat Transfer A*, vol. 52, pp. 377–397, 2007.

13. N. Yucel and R. T. Guven, Forced-Convection Cooling Enhancement of Heated Elements in a Parallel-Plate Channels Using Porous Inserts, *Numer. Heat Transfer A*, vol. 51, pp. 293–312, 2007.

14. J. Eriksson, S. Ormarsson, and H. Petersson, Finite-Element Analysis of Coupled Nonlinear Heat and Moisture Transfer in Wood, *Numer. Heat Transfer A*, vol. 50, pp. 851–864, 2006.

15. S. C. Hirata, B. Goyeau, D. Gobin, and R. M. Cotta, Stability of Natural Convection in Superposed Fluid and Porous Layers Using Integral Transforms, *Numer. Heat Transfer B*, vol. 50, pp. 409–424, 2006.

16. L. Betchen, A. G. Straatman, and B. E. Thompson, A Nonequilibrium Finite-Volume Model for Conjugate Fluid/Porous/Solid Domains, *Numer. Heat Transfer A*, vol. 49, pp. 543–565, 2006.

17. Y. W. Zhang, Nonequilibrium Modeling of Heat Transfer in a Gas-Saturated Powder Layer Subject to a Short-Pulsed Heat Source, *Numer. Heat Transfer A*, vol. 50, pp. 509–524, 2006.

18. X. H. Wang, M. Quintard, and G. Darche, Adaptive Mesh Refinement for One-Dimensional Three-Phase Flow with Phase Change in Porous Media, *Numer. Heat Transfer B*, vol. 50, pp. 231–268, 2006.

19. X. H. Wang, M. Quintard, and G. Darche, Adaptive Mesh Refinement for One-Dimensional Three-Phase Flow with Phase Change in Porous Media, *Numer. Heat Transfer A*, vol. 50, pp. 315–352, 2006.

20. C. R. Ruivo, J. J. Costa, and A. R. Figueiredo, Analysis of Simplifying Assumptions for the Numerical Modeling of the Heat and Mass Transfer in a Porous Desiccant Medium, *Numer. Heat Transfer A*, vol. 49, pp. 851–872, 2006.

21. F. Moukalled and Y. Saleh, Heat and Mass Transfer in Moist Soil, Part I. Formulation and Testing, *Numer. Heat Transfer A*, vol. 49, pp. 467–486, 2006.

22. A. Mansour, A. Amahmid, M. Hasnaoui, and M. Bourich, Multiplicity of Solutions Induced by Thermosolutal Convection in a Square Porous Cavity Heated from Below and Submitted to Horizontal Concentration Gradient in the Presence of Soret Effect, *Numer. Heat Transfer A*, vol. 49, pp. 69–94, 2006.

23. A. V. Kuznetsov, L. Cheng, and M. Xiong, Effects of Thermal Dispersion and Turbulence in Forced Convection in a Composite Parallel-Plate Channel: Investigation of Constant Wall Heat Flux and Constant Wall Temperature Cases, *Numer. Heat Transfer A*, vol. 42, pp. 365–383, 2002.

24. B. M. D. Miranda and N. K. Anand, Convective Heat Transfer in a Channel with Porous Baffles, *Numer. Heat Transfer A*, vol. 46, pp. 425–452, 2004.

25. N. B. Santos and M. J. S. de Lemos, Flow and Heat Transfer in a Parallel-Plate Channel with Porous and Solid Baffles, *Numer. Heat Transfer A*, vol. 49, pp. 471–494, 2006.

26. S. Y. Kim and A. V. Kuznetsov, Optimization of Pin-Fin Heat Sinks Using Anisotropic Local Thermal Nonequilibrium Porous Model in a Jet Impinging Channel, *Numer. Heat Transfer A*, vol. 44, pp. 771–787, 2003.

27. M. Prakash, F. O. Turan, Y. Li, J. Manhoney, and G. R. Thorpe, Impinging Round Jet Studies in a Cylindrical Enclosure with and without a Porous Layer: Part I: Flow Visualisations and Simulations, *Chem. Eng. Sci.*, vol. 56, pp. 3855–3878, 2001.

28. M. Prakash, F. O. Turan, Y. Li, J. Manhoney, and G. R. Thorpe, Impinging Round Jet Studies in a Cilindrical Enclosure with and without a Porous Layer: Part II: LDV Measurements and Simulations, *Chem. Eng. Sci.*, vol. 56, pp. 3879–3892, 2001.

29. W.-S. Fu and H.-C. Huang, Thermal Performance of Different Shape Porous Blocks under an Impinging Jet, *Int. J. Heat Mass Transfer*, vol. 40, pp. 2261–2272, 1997.

30. M. H. J. Pedras and M. J. S. de Lemos, Macroscopic Turbulence Modeling for Incompressible Flow through Undeformable Porous Media, *Int. J. Heat Mass Transfer*, vol. 44, pp. 1081–1093, 2001.

31. M. H. J. Pedras and M. J. S. de Lemos, Computation of Turbulent Flow in Porous Media Using a Low-Reynolds k-Epsilon Model and an Infinite Array of Transversally Displaced Elliptic Rods, *Numer. Heat Transfer A*, vol. 43, pp. 585–602, 2003.

32. F. D. Rocamora Jr. and M. J. S. de Lemos, Analysis of Convective Heat Transfer of Turbulent Flow in Saturated Porous Media, *Int. Commun. Heat Mass Transfer*, vol. 27, pp. 825–834, 2000.

33. M. J. S. de Lemos and E. J. Braga, Modeling of Turbulent Natural Convection Porous Media, *Int. Commun. Heat Mass Transfer*, vol. 30, pp. 615–624, 2003.

34. E. J. Braga and M. J. S. de Lemos, Turbulent Natural Convection in a Porous Square Cavity Computed with a Macroscopic k-ε Model, *Int. J. Heat Mass Transfer*, vol. 47, pp. 5639–5650, 2004.

35. E. J. Braga and M. J. S. de Lemos, Heat Transfer in Enclosures Having a Fixed Amount of Solid Material Simulated with Heterogeneous and Homogeneous Models, *Int. J. Heat Mass Transfer*, vol. 48, pp. 4748–4765, 2005.

36. E. J. Braga and M. J. S. de Lemos, Turbulent Heat Transfer in an Enclosure with a Horizontal Porous Plate in the Middle, *J. Heat Transfer*, vol. 128, pp. 1122–1129, 2006.

37. E. J. Braga and M. J. S. de Lemos, Simulation of Turbulent Natural Convection in a Porous Cylindrical Annulus Using a Macroscopic Two-Equation Model, *Int. J. Heat Mass Transfer*, vol. 49, pp. 4340–4351, 2006.

38. M. J. S. de Lemos and M. S. Mesquita, Turbulent Mass Transport in Saturated Rigid Porous Media, *Int. Commun. Heat Mass Transfer*, vol. 30, pp. 105–113, 2003.

39. M. B. Saito and M. J. S. de Lemos, Interfacial Heat Transfer Coefficient for Non-equilibrium Convective Transport in Porous Media, *Int. Commun. Heat Mass Transfer*, vol. 32, pp. 666–676, 2005.

40. M. B. Saito and M. J. S. de Lemos, A Correlation for Interfacial Heat Transfer Coefficient for Turbulent Flow over an Array of Square Rods, *J. Heat Transfer*, vol. 128, pp. 444–452, 2006.

41. M. J. S. de Lemos and L. A. Tofaneli, Modeling of Double-Diffusive Turbulent Natural Convection in Porous Media, *Int. J. Heat Mass Transfer*, vol. 47, pp. 4233–4241, 2004.

42. M. J. S. de Lemos and M. H. J. Pedras, Recent Mathematical Models for Turbulent Flow for Saturated Rigid Porous Media, *J. Fluids Eng.*, vol. 123, pp. 935–940, 2001.

43. M. J. S. de Lemos, Fundamentals of the Double-Decomposition Concept for Turbulent Transport in Permeable Media, *Materialwiss. Werkstoff.*, vol. 36, pp. 586–593, 2005.

44. M. J. S. de Lemos, Turbulent Kinetic Energy Distribution Across the Interface Between a Porous Medium and a Clear Region, *Int. Commun. Heat Mass Transfer*, vol. 32, pp. 107–115, 2005.

45. M. Assato, M. H. J. Pedras, and M. J. S. de Lemos, Numerical Solution of Turbulent Channel Flow Past a Backward-Facing Step with a Porous Insert Using Linear and Nonlinear k–Epsilon Models, *J. Porous Media*, vol. 8, pp. 13–29, 2005.

46. M. J. S. de Lemos and R. A. Silva, Turbulent Flow Over a Layer of a Highly Permeable Medium Simulated with a Diffusion-Jump Model for the Interface, *Int. J. Heat Mass Transfer*, vol. 49, pp. 546–556, 2006.

47. W. G. Gray and P. C. Y. Lee, On the Theorems for Local Volume Averaging of Multiphase System, *Int. J. Multiphase Flow*, vol. 12, pp. 401–410, 1977.
48. S. V. Patankar, *Numerical Heat Transfer and Fluid Flow*, Hemisphere, New York, 1980.
49. A. R. P. Heiningen, A. S. Mujumdar, and W. J. M. Douglas, Numerical Prediction of the Flow Field and Impingement Heat Transfer Due to a Laminar Slot Jet, *J. Heat Transfer*, vol. 98, pp. 654–658, 1976.
50. K. M. Kelkar and S. V. Patankar, Numerical Prediction of Flow and Heat Transfer in a Parallel Plate Channel with Staggered Fins, *J. Heat Transfer*, vol. 109, pp. 25–30, 1987.